Environmental Nanotechnology, Monitoring & Management 25 (2026) 101134

Contents lists available at ScienceDirect

Environmental Nanotechnology, Monitoring & Management

journal homepage: www.elsevier.com/locate/enmm

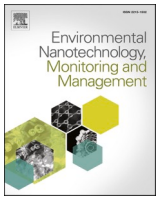

Development of a whey protein adsorbent via a novel green electrospinning process: Optimization of synthesis parameters and evaluation of lead removal from water

Mateo Gallardo-Salas [a], María Ximena Quintanilla-Carvajal [b], Didilia Ileana Mendoza-Castillo [c,d], Adrián Bonilla-Petriciolet [d], Martha Cobo [e], Carlos Jiménez-Junca [a,*]

[a] Research Group in Bioprospecting, Universidad de La Sabana, Chía 250001, Colombia
[b] Research Group in Agroindustrial Processes, Universidad de La Sabana, Chía 250001, Colombia
[c] Secretaría de Ciencia, Humanidades, Tecnología e Innovación, Ciudad de México 03940, Mexico
[d] Tecnológico Nacional de México, Instituto Tecnológico de Aguascalientes, Aguascalientes 20256, Mexico
[e] Energy, Materials and Environment Laboratory, Universidad de La Sabana, Chía 250001, Colombia

ARTICLE INFO

Keywords:
Adsorption
Bromelain
Green electrospinning
Nanofibers
Whey protein

ABSTRACT

Electrospun nanofibers are increasingly used in environmental applications, particularly for water remediation, but their sustainability is limited by the reliance on toxic organic solvents. This study investigates the electrospinning of a blended solution of whey protein fibrils (WPF), a residual by-product of the dairy industry, and polycaprolactone (PCL), using bromelain hydrolysis and green solvents to obtain nanofibers for the removal of lead (Pb) from water. Defect-free nanofibers with mean diameter of 97 nm were synthesized by optimization of polymer solution parameters and electrospinning conditions, with solution viscosity as a means to predict spinnability via the entanglement concentration. FT-IR, SEM-EDX, XRD and XPS analyses revealed that WPF/PCL fibers are rich in amine, amide, and oxygenated functional groups, facilitating lead adsorption through chemical complexation and physical interactions. Kinetic studies revealed that the pseudo-second-order model was the best fit for experimental data, with an equilibrium time of 4 h. Adsorption isotherms showed that the experimental data followed the Langmuir model, with a maximum adsorption capacity of 0.35 mmol g^{-1}, while the thermodynamic analysis established the endothermicity of the adsorption. These results highlight the potential of whey protein and green electrospinning to produce nanofibers for heavy metal removal from water without a complex and environmentally harmful production process.

1. Introduction

Despite global efforts to manage water resources safely, increasing water demand from industrialization and urbanization continues to strain water quality, especially in lower-income countries with inadequate wastewater treatment infrastructure for emerging contaminants such as pharmaceuticals, microplastics, and heavy metals (HMs) (Acosta-González et al., 2025; UNESCO, 2024). Among these, HMs are of significant concern due to their ability to bioaccumulate in different organisms and potential for biomagnification (Biedunkova and Kuznietsov, 2025). Lead (Pb) is recognized as a priority heavy metal by the World Health Organization (WHO) because of its acute toxicity and extensive use in anthropogenic activities, which can lead to disruptions in the neurological, reproductive and cardiovascular systems (Collin et al., 2022; Saisree et al., 2025). Efforts to mitigate Pb pollution include development of improved technologies such as adsorption, valued for its high efficiency and simplicity (Liang et al., 2022). Traditional adsorbents suffer from high production and regeneration costs, complex pretreatment, and poor scalability, especially as the majority of adsorbents reported in the literature are used as powders (Du et al., 2024). As such, there is a need to develop sustainable and inexpensive materials with high adsorption properties.

Electrospun fibers have recently emerged as a promising approach for water treatment, as they overcome the main drawbacks of powdered adsorbents and enable higher flux rates in continuous adsorption processes (Mohamed et al., 2025). Electrospinning is an

* Corresponding author.
E-mail address: carlosjj@unisabana.edu.co (C. Jiménez-Junca).

https://doi.org/10.1016/j.enmm.2026.101134
Received 28 November 2025; Received in revised form 9 February 2026; Accepted 13 February 2026
Available online 15 February 2026

electrohydrodynamic process in which a polymer solution is subjected to an electric field induced by a high-voltage power supply. At critical voltage, the electrostatic forces of the droplet overcome its stabilizing surface tension, leading to ejection of the solution in the form of a Taylor cone. As the jet is attracted and further stretched to a grounded metal collector, the solvent gradually evaporates, and ultrafine dry solidified fibers are deposited (Kutzli et al., 2019; Zhu et al., 2021). Successful spinning of fibers with no defects, e.g. beads, droplets, or ribbon-like structures, depends on several interrelated variables: environmental parameters, equipment operating parameters (applied voltage, solution flow rate, and distance from tip to collector), and solution parameters (solution viscosity, conductivity, surface tension, and solvent polarity). Molecular interactions between the polymer and solvent, expressed by the parameters of the solution, have been proven by several authors as the driving factor behind the electrostatic and fluid dynamics forces governing the morphology and structure of electrospun fibers (Chen et al., 2025; Munawar et al., 2025). Indeed, while the selected polymer must allow sufficient chain interactions to form an "entangled regime" (Wilk, 2021), the solvent must ensure a low solubility parameter distance (Behroozi et al., 2023), low conductivity, and high volatility (Rostami et al., 2023), which has led high-molecular-weight petroleum-derived polymers and volatile organic solvents as the templates for electrospinning. However, this system can compromise the safety and sustainability of the process due to the carbon footprint of the polymer and toxicity and disposal issues associated with the solvent (Wang et al., 2024).

Natural biopolymers have garnered attention as sustainable alternatives to synthetic polymers owing to their availability and biodegradability (Perez-Puyana et al., 2025). Whey protein is a particularly attractive biopolymer due to its functional properties, high amino acid profile, and low cost, as it is an abundant by-product of cheese production often discharged to water bodies without treatment (Ali et al., 2023; Li et al., 2025). According to FAO (2025), international trade in cheese reached 3.7 million tons in 2024, thus generating almost 167 million m^3 of whey, considering a production rate of 9 L of whey per kg of cheese. Whey management strategies are particularly lacking in developing-countries, with reports claiming around 50% of whey volume is discarded, resulting in changes in soil structure and eutrophication in water systems (Casallas-Ojeda et al., 2024; Uribe-Velázquez et al., 2025). As such, whey can be repurposed via different valorization processes and contribute to the circular economy concept, notably as a precursor for the development of bio-adsorbents for HMs remediation. Indeed, several authors have reported the metal binding capacities of whey proteins, namely β-lactoglobulin (β-Lg) and α-lactalbumin (α-La), due to their richness in functional groups that serve as active sites for HMs (Soon et al., 2022; Zhu et al., 2021). However, their globular conformation and weak intermolecular interactions inhibit sufficient chain entanglements and charge accumulation, leading to larger aggregates or droplets, a characteristic of electrospraying rather than electrospinning (Drosou et al., 2018; Wilk, 2021). The spinnability of this protein can be improved through protein denaturation or blending with complementary spinnable polymers, as shown by Ramírez-Rodríguez et al. (2023), who obtained electrospun nanofibers using a 18 wt% whey protein-polycaprolactone (PCL) solution in tetrahydrofuran (THF) and N,N-dimethylformamide (DMF). These organic solvents carry a considerable environmental footprint that can be reduced by replacing them with benign options, such as methanol, ethanol, acetic acid (AA), or formic acid (FA), classified as green solvents by the environmental, health, and safety (EHS) indicator and the life-cycle assessment (LCA) method, exemplifying the promise of green electrospinning (Avossa et al., 2022). Similarly, replacing toxic denaturation agents, such as β-mercaptoethanol (β-Me), with naturally derived sources that disrupt the globular nature of proteins can further enhance the sustainability and safety of the electrospinning process. For instance, tannic acid has been showed to modulate oat protein structure to form amyloid fibrils for quercetin encapsulation (Xu et al., 2025), while Fu et al. (2025) reported that bromelain, a cysteine endopeptidase, promotes the formation of fibrillar aggregates of quinoa protein. Relative to other fibrillation inducers, an added benefit of bromelain is that it can be extracted and isolated from pineapple residues (Li et al., 2021).

This study reports the development of nanofibers produced by green electrospinning of different blends of whey protein fibrils (WPF) and polycaprolactone. To the best of our knowledge, to date no studies have reported the fibrillation of whey proteins using bromelain, nor the successful spinning of these polymers in green solvents. The nanofibers exhibiting the most uniform morphology and smallest diameter were selected for the investigation of Pb removal from water. Therefore, this work aims to bridge the gap in green electrospinning of biopolymers such as whey protein for remediation applications, while promoting sustainable adsorbent design by coupling waste valorization, safer processing conditions with reduced solvent hazard, and effective heavy metal removal from water.

2. Experimental

2.1. Materials

The materials and reagents used in this study, along with their sources, are listed in the supplementary material (Section S1.1).

2.2. Enzymatic hydrolysis with bromelain

To perform enzymatic hydrolysis, whey protein isolate (WPI) was dissolved into a 100 mM phosphate-buffered saline (PBS) solution at pH 7.0 and incubated at 50 °C for 10 min in a thermostatic shaker (New Brunswick Scientific Innova 42, USA) at 150 rpm. Temperature and pH conditions were used in accordance with previous studies related to optimal bromelain activity on several substrates, including whey protein (Corzo et al., 2012; Du et al., 2022; Li et al., 2021; Ricaurte et al., 2020). The enzyme-to-substrate volume ratio was maintained at 0.02 wt/vol%. The reaction was conducted at 50 °C for another 40 min and thereafter adjusted to ~pH 1.1 by adding 0.1 M HNO_3 to stop further denaturation. Samples were then lyophilized and stored at −4 °C until subsequent use.

2.3. Characterization of enzymatic-denatured whey protein

The proteolytic activity of crude bromelain on whey protein was determined according to Cupp-Enyard (2008). Briefly, bromelain was incorporated in a 100 mM PBS solution containing 0.65 wt/vol% WPI and incubated at process conditions mentioned in Section 2.2. Aliquots (2 mL) of the supernatant were mixed with 5 mL of 0.5 M Na_2CO_3 and 1 mL of Folin's reagent, mixed with vortex and incubated again at 37 °C for 30 min. Absorbance of samples was measured at 655 nm using a spectrophotometer (BioRad iMark Microplate Reader, USA). Bromelain activity was calculated using eq. S1 (Section S1.2 of the supplementary material). Fibrillation of enzymatic-denatured whey was validated by the Congo red (CR) binding assay, as reported by Yang et al. (2023).

2.4. Preparation of electrospinning solutions and electrospinning conditions

A solvent mixture of formic acid and acetic acid was prepared at a mixing ratio of 2:3 (v/v) to obtain the electrospinning solutions. Corresponding amounts of WPF powder and PCL were dissolved in 25 mL of solvent and stirred at room temperature (RT) at 400 rpm for 2 h, ensuring a transparent solution. Composite fibers were obtained using an electrospinning equipment (Bioinicia Fluidnatek LE-10, Spain) at RT, relative humidity of 30%, flow rate of 3 mL h^{-1} set on a 10 mL plastic syringe and a high-voltage supply in the range of 15–20 kV. Solutions mass loadings (WPF and PCL concentrations) and tip-to-collector distance were assessed as independent factors of a Box-Behnken experimental design to optimize fiber formation, as shown in Table 1.

Table 1
Independent variables and levels used in the Box-Behnken experimental design.

Coded values	Independent variables	Levels		
		−1	0	+1
x_1	WPF concentration (wt%)	2	4	6
x_2	PCL concentration (wt%)	1	2	3
x_3	Collector distance (cm)	5	9	13

2.5. Solution and nanofiber characterization

Apparent viscosity, surface tension, and electrical conductivity of electrospinning solutions were measured as described in Section S1.3 of the supplementary material. All measurements were performed in triplicate using different samples to ensure accuracy. Fiber morphology was observed by scanning electron microscopy (SEM) using a high-resolution microscope (TESCAN LYRA3, Czech Republic) with an acceleration voltage of 10 kV. For each image, at least 100 different fibers were randomly selected and measured using the ImageJ software, so that mean diameter was reported from 3 images per run. Along with the SEM observation, fibers were subjected to energy-dispersive X-ray spectroscopy (EDX) to determine their elemental composition.

2.6. Optimal nanofiber characterization

The physico-chemical properties of WPF/PCL fibers were analyzed using Fourier-transform infrared spectroscopy (FT-IR), X-ray diffraction (XRD), nitrogen physisorption measurements, and X-ray photoelectron spectroscopy (XPS). The pH at the point of zero charge (pH_{pzc}) was determined via the salt addition method, while the water contact angle was assessed via the sessile drop method. Detailed characterization procedures are provided in Section S1.4 of the supplementary material.

2.7. Batch adsorption experiments

Lead removal performance of WPF/PCL nanofibers was evaluated using aqueous solutions of Pb^{2+} by batch experiments under various operational conditions, such as solution pH, initial adsorbate concentration, contact time, and temperature. The electrospun adsorbent was added to the adsorbate solution at a dosage (AD) of 4 g L^{-1} and stirred at 180 rpm using a thermostatic shaker (LabTech LSB-0155, Korea). The heavy metal concentration in the liquid phase was determined by atomic absorption spectroscopy (Thermo Fisher Scientific iCE 3000, Germany). The adsorption capacity was calculated using the following mass balance equation (Eq. 1):

$$q_e = \frac{(C_0 - C_e)V}{m_s} \quad (1)$$

Where C_0 and C_e are the initial and equilibrium concentrations of Pb^{2+} (mmol L^{-1}), respectively; V is the solution volume (L); and m_s is the WPF/PCL adsorbent mass (g) used in the experiments. Solution pH that favored the best adsorbent performance (i.e., pH 5) was used to analyze the prepared composite's adsorption equilibrium time and maximum adsorption capacity. All adsorption experiments were performed in triplicate, including a blank to ensure data reproducibility.

2.7.1. Adsorption kinetics

For kinetic experiments, two initial Pb^{2+} concentrations were evaluated (0.72 and 1.69 mmol L^{-1}) at pH 5 and 30 °C. Samples were withdrawn from the thermal bath at specified time intervals (0.5–24 h). The pseudo-first order (PFO), pseudo-second order (PSO), and Elovich models (Table S1) were employed to calculate the adsorption kinetic constants and to model the experimental data. Data correlation was explored via non-linear regression analysis using the determination coefficient (R^2) and root mean squared error (*RMSE*).

2.7.2. Adsorption isotherms

For the adsorption equilibrium study, initial Pb^{2+} concentrations of 0.27–5.34 mmol L^{-1} were used to quantify the isotherms at 20 and 30 °C, respectively. Experimental data were assessed with two-parameter (Langmuir, Freundlich, and Dubinin-Radushkevich) and three-parameter (Sips, Redlich-Peterson, and Toth) theoretical isotherm models (Table S2). Model suitability was evaluated as described for the kinetic experiments.

2.8. Statistical analysis

A response surface methodology (RSM) was applied for the experimental design described in Section 2.4 using the software Design-Expert version 10 (Stat-Ease Inc., USA). The data were analyzed using multiple regressions with the least squares method, and R^2 and lack-of-fit values determined the model fit. A *t*-test was conducted to determine the differences between treatments.

3. Results and discussion

3.1. Effect of bromelain on WPI

Proteolytic activity of stem bromelain determined with whey protein was significantly higher than with gelatin (control) (Fig. S1a), mainly due to higher content of aromatic and hydrophobic amino acids of WPI (Rout et al., 2024). The control was also used to validate the theoretical activity of the enzyme (1200 GDU), showing only a 20% activity loss. Moreover, this assay was conducted on WPI with β-Me instead of bromelain, as it is a reducing agent that cleaves disulfide bonds and disrupts the quaternary structure of proteins (Nguyen et al., 2012). As seen in Fig. S1a, the amount of tyrosine equivalents released from WPI treated with β-Me (4.0±0.0 U mL^{-1}) was comparable to that of WPI treated with bromelain (3.4±0.1 U mL^{-1}). This may be due to the similar mechanisms of both denaturation agents, which are based on thiol interactions within peptide bonds (Bustamante et al., 2022; Li et al., 2021). However, bromelain has the advantages of bioavailability and non-toxicity, as β-Me can be toxic if inhaled or ingested (Foroumadi and Saeedi, 2014). These results suggest that enzymatic hydrolysis with bromelain induce the generation of protein aggregates that are prone to β-sheet stacking and subsequent fibrillation (Aceituno-Medina et al., 2013). Indeed, presence of fibrils was confirmed by Congo red absorption spectra in the WPI treated with bromelain (WPF), as observed via the increase of intensity and the redshift from the CR peak at 490 nm to 510 nm (Fig. S1b) (Yang et al., 2023). These results are in line with the work of Fu et al. (2025), who reported enzyme denaturation of quinoa protein, which has a similar amino acid profile compared to whey (Dakhili et al., 2019). As such, this study highlights the potential of bromelain to induce fibrillation, providing a novel approach to obtain whey fibrils for different applications.

3.2. Characterization of electrospinning solutions

Surface tension remained almost constant for the different mass loadings of WPF and PCL, with total polymer concentration having no significant effect ($p<0.05$). However, increasing the whey fibrils content from 2 to 6 wt% and increasing the PCL content from 1 to 3 wt% led to lower surface tension values (Table 2). This trend aligns with the results reported by Ali et al. (2023) and Saghaee et al. (2025), who noted the decrement of surface tension with increasing protein content in whey blended with different co-spinning polymers (polyvinyl alcohol and pullulan). The lower surface tension can be attributed to partial unfolding of whey proteins from the bromelain treatment, favoring the exposure and migration of hydrophobic groups to the solution's surface (Stie et al., 2022). A higher mass ratio of PCL also led to greater solution hydrophobicity due to its ester group. Moreover, the behavior of this solution parameter can be related to a high polymer–solvent affinity and

Table 2
Surface tension, electrical conductivity, apparent viscosity at a shear rate of 50 s^{-1}, and power law indices K and *n* of electrospinning solutions prepared from whey protein fibrils (WPF) and polycaprolactone (PCL).

Sample	WPF:PCL ratio (% w/w)	Surface tension (mN/m)	Electrical conductivity (mS/cm)	Apparent viscosity (mPa·s)	K (Pa·s^n)	n	R^2	RMSE
A	0:0	30.82 ± 0.01^{a}	0.12 ± 0.00^{a}	1.76 ± 0.51^{a}	0.002 ± 0.000^{a}	0.94 ± 0.00^{a}	>0.99	0.00
B	2:1	31.19 ± 0.05^{b}	0.76 ± 0.01^{b}	7.85 ± 0.96^{b}	0.007 ± 0.000^{b}	1.01 ± 0.00^{b}	1.00	0.00
C	2:2	31.12 ± 0.04^{b}	0.67 ± 0.02^{c}	16.69 ± 1.24^{cd}	0.017 ± 0.000^{c}	1.00 ± 0.00^{b}	1.00	0.00
D	2:3	30.78 ± 0.03^{a}	0.55 ± 0.00^{d}	29.52 ± 2.23^{e}	0.028 ± 0.000^{d}	0.99 ± 0.00^{b}	1.00	0.00
E	4:1	31.14 ± 0.02^{b}	1.15 ± 0.01^{e}	11.88 ± 0.93^{c}	0.011 ± 0.000^{e}	1.00 ± 0.00^{b}	1.00	0.00
F	4:2	31.02 ± 0.06^{b}	1.09 ± 0.01^{f}	19.24 ± 2.61^{de}	0.024 ± 0.000^{f}	0.98 ± 0.00^{c}	1.00	0.00
G	4:3	30.83 ± 0.04^{a}	0.90 ± 0.01^{g}	45.16 ± 2.21^{g}	0.048 ± 0.000^{g}	0.97 ± 0.00^{d}	1.00	0.00
H	6:1	31.14 ± 0.10^{b}	1.53 ± 0.01^{h}	23.28 ± 1.98^{d}	0.020 ± 0.000^{h}	0.98 ± 0.00^{c}	1.00	0.00
I	6:2	30.98 ± 0.01^{b}	1.40 ± 0.02^{i}	36.52 ± 1.69^{f}	0.042 ± 0.000^{i}	0.94 ± 0.00^{a}	1.00	0.00
J	6:3	30.80 ± 0.03^{a}	1.39 ± 0.01^{i}	94.74 ± 3.07^{h}	0.151 ± 0.001^{j}	0.87 ± 0.00^{e}	>0.99	0.01

Results expressed as the mean±standard deviation of three independent experiments. Different letters indicate significant difference ($p<0.05$) between samples. Abbreviations: K, consistency index; *n*, flow behavior index; R^2, determination coefficient; RMSE, root mean square error.

compatibility between polymers (Wu et al., 2023).

As shown in Table 2, the electrical conductivity increased significantly ($p<0.05$) with increasing mass concentration, particularly for whey protein, which achieved the highest conductivity range of 1400–1550 μS/cm for solutions containing 6 wt% of WPF. This aligns with the findings from Kutzli et al. (2019) and (Zhao et al., 2023). Whey proteins possess carboxylic and amine groups that can be positively charged when the solution pH is lower than their isoelectric point (~5.0) (Aman mohammadi et al., 2019). Herein, the solvent blend of formic and acetic acid is not only crucial for the proper solvation of polymer molecules, but also for maintaining an acidic medium (pH=2.5), where protonation of whey proteins enhances the solution's conductivity. Conversely, increasing the proportion of PCL resulted in an overall decrease in electrical conductivity due to its molecular interaction with WPF; the weaker ionic nature of PCL diminished the polyelectrolyte properties of protein fibrils (Ali et al., 2023).

Apparent viscosity exhibited a similar trend; increasing the solids concentration in the blend formulation resulted in significantly more viscous solutions ($p<0.05$), with PCL demonstrating a more pronounced effect on viscosity than WPF. As illustrated in Fig. 1, all samples exhibited shear rate dependence, as the viscosity decreased with increasing shear rate, which is characteristic of a non-Newtonian pseudoplastic fluid. Shear thinning behavior was confirmed with the rheological parameters obtained by fitting the power-law model to the experimental data ($R^2>0.99$), as presented in Table 2. The flow index of solutions with a total solids concentration below 5 wt% did not change significantly. In contrast, the power-law *n* value of solutions with higher polymer concentrations decreased significantly ($p<0.05$), from 0.98 for sample F to 0.87 for sample J, suggesting that TDS>6 wt% leads to solutions more susceptible to shear stress. On the other hand, the consistency coefficient of these samples (F-J) increased significantly, reflecting a greater extent of intermolecular interactions, unfolding of whey proteins, chain entanglements, and formation of new molecular networks (Saghaee et al., 2025). Therefore, the combination of 2 wt% of WPF and 2 wt% of PCL can be regarded as the entanglement concentration (C_{etg}) (Fig. S2); production of uniform fibers requires that the solution concentration to be approximately 1.2–2.0 times the entanglement concentration (Perez-Puyana et al., 2025). Based on this, a total polymer concentration of 5 wt% should represent a good starting point for achieving uniform spinnability.

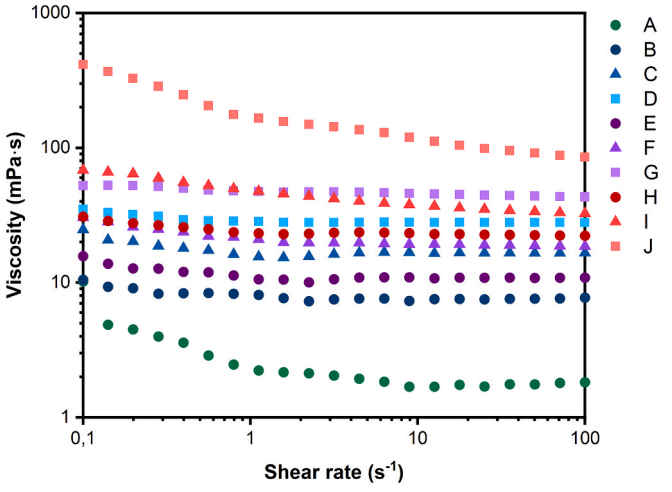

Fig. 1. Apparent viscosities of WPF:PCL blend solutions at different mass loadings as a function of shear rate.

3.3. Correlation of solution properties with morphology of fibers

Solutions of whey proteins, whether in their native or denatured state, did not yield fibers under any set of process conditions, even at the highest possible voltage applied (25 kV). The behavior of the solution during electrospinning was characterized by droplet collapse at the needle tip and jet breakage in the Taylor cone, leading to the deposition of deformed droplets on the collector (Fig. S3). The lack of spinnability of native whey can be attributed to the closely-packed globular structure of its main proteins, which do not promote sufficient polymer interactions (Zhang et al., 2023). Even after hydrolysis and disruption of polypeptide chains of WPI, the entanglement regime is not achieved due to its low molecular weight (β-Lg: 17 kDa, α-La: 14 kDa) compared to other spinnable polymers (MW>30 kDa) (Avossa et al., 2022).

In contrast, different morphologies were obtained with the inclusion of PCL at different polymer mass ratios and tip-collector distances, as shown in their respective SEM images (Fig. 2). Sprayed particles were generated at WPF-to-PCL mass ratios of 2:1 (run 1) and 4:1 (runs 2 and

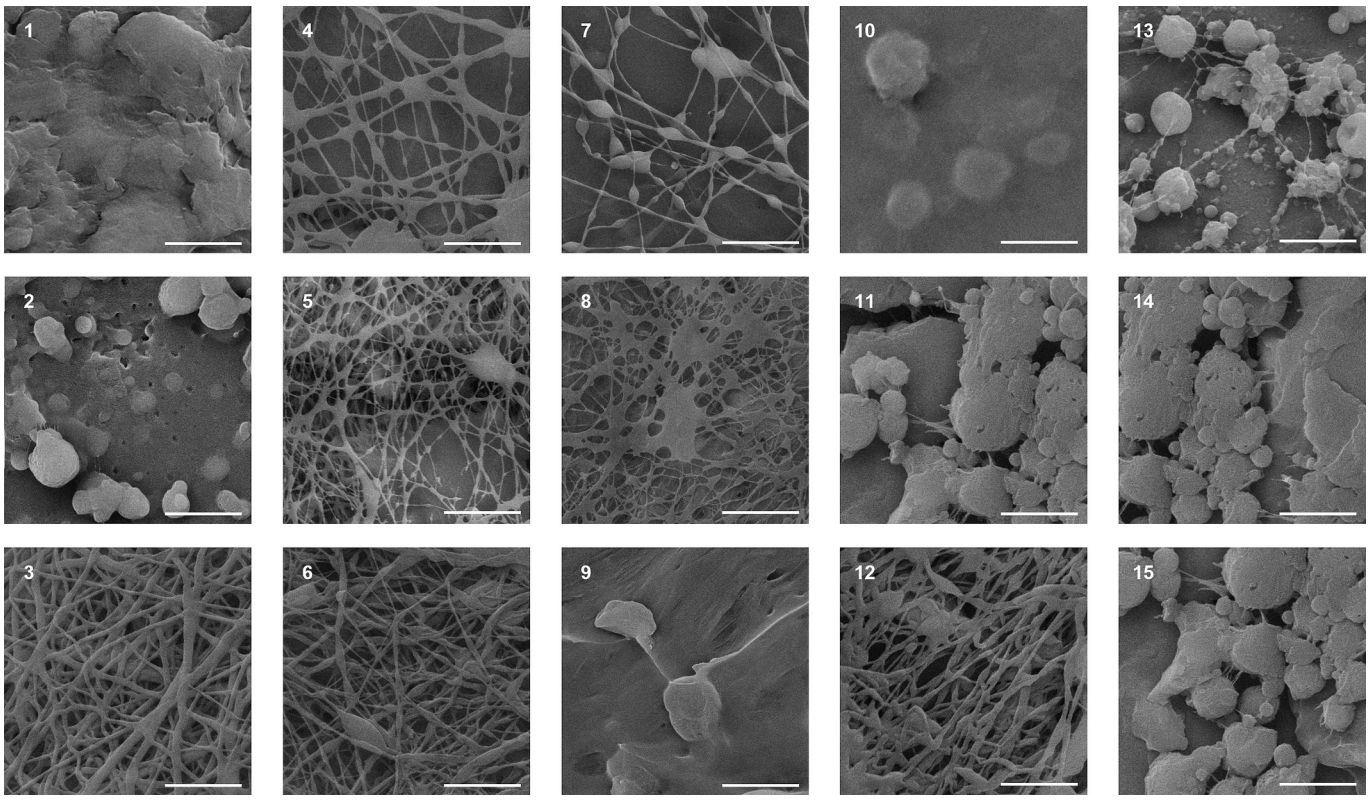

Fig. 2. SEM images of electrospun WPF:PCL solutions at different concentrations and tip-collector distances according to Box-Behnken experimental design runs (1–15). All images share the same scale bar: 2 μm.

10), regardless of collector distance. These defects were ascribed to the physical properties of the solutions, because they presented the highest surface tension values and lowest viscosities (Table 2). This high surface tension may overcome the electrostatic forces, and with low viscoelasticity, the Rayleigh instability is not suppressed, preventing the formation of continuous fibers (Rostamabadi et al., 2020). An increase in the PCL concentration to 2 wt% led to the formation of droplets with tiny fibers due to increased viscosity (runs 11, 14 and 15), generating enough stress to stretch the solution in the electric field (Behroozi et al., 2023). Fibers with web-like patterns and flattened spots emerged at 2:2 WPF: PCL mass ratio spun at a distance of 5 cm (run 8/solution C), which confirms that C_{etg} can be used to predict spinnability of polymer solutions, despite the presence of some defects. This solution was also spun at a larger tip-to-collector distance (13 cm, run 9), obtaining beaded defects. These differences in morphology indicate that an insufficient jet flight duration exists at shorter distances to allow for solvent evaporation, whereas longer distances reduce the forces stabilizing the jet (Refate et al., 2023). Conversely, the WPF:PCL blend at a proportion of 6:1 (run 13) yielded beaded fibers, even though its concentration was higher than the entanglement concentration mentioned in Section 3.2. The high conductivity of this solution (1530 μS/cm) can explain this behavior, as it leads to a higher charge density in the Taylor cone, which breaks up the jet into a polydisperse spray. High-conductivity solutions are often preferred in this field because they encourage greater elongation of the jet along its axis, thereby producing finer electrospun mats. However, if the conductivity is too high, the solution becomes unstable and forms heterogenous structures (Soleimanifar et al., 2020; Zhao et al., 2023), as observed in this study.

Clear fibers started to appear in the composite morphology when the solution viscosity was higher than 23 mPa·s (runs 3, 4, 5, 6, 7, and 12), as in the blends with mass concentrations above the C_{etg}, as predicted in Section 3.2. At a PCL solution concentration of 3 wt%, the electrospun material obtained had relatively well-distributed, continuous and beadless fibers. In these samples, increasing the concentration of WPF resulted in a reduction of spindle-like structures and formation of more homogeneous linear fibers, although with a more ribbon-like structure. This can be associated with the lower viscosity of the 2:3 and 4:3 WPF: PCL mass ratios (solutions D and G, respectively), as they had insufficient molecular entanglement to complete jet stretching (Saghaee et al., 2025). The significantly higher shear-thinning behavior of the 6:3 blend (power-law n values from Table 2) also favors jet initiation and stretching of this solution into more uniform fibers at the shear rate of the Taylor cone, approximately 800 to 1200 s^{-1} (Lv et al., 2025). Moreover, its higher conductivity means that this solution could carry more electric charge and thus reduce the collected fibers diameters (Chen et al., 2025). The non-significant differences in the surface tension values of these precursor blends implied that viscoelastic and electrostatic forces overcame the cohesive forces of the solutions and primarily control fiber morphology, which was confirmed by the changes in mean diameter observed in Table 3.

Our results align with those of Lv et al. (2025) and Ayazi et al. (2024), emphasizing the importance of solution parameters in predicting morphological properties. Other studies investigating the spinnability of whey proteins with other co-spinning polymers (Ahmed et al., 2016; Kutzli et al., 2019; Zhong et al., 2018) found comparable average diameters ranging from 100 to 400 nm, along with a correlation between solution properties and morphology. However, in this study, this biopolymer could be spined without the use of any organic solvent, partly because of the enzymatic pretreatment of bromelain, as discussed in Section 3.1. Indeed, without denaturation the viscosity at 50 s^{-1} of a 6:3 blend of WPI and PCL was 129.6±4.2 mPa·s, 30% higher than the viscosity of the same solution with whey fibrils, which did not even form the Taylor cone and only resulted in broken droplets. In general, all electrospun mats depicted smooth surfaces, which indicated suitable interactions between WPF and PCL, along with a strong affinity between the blend of polymers and the solvent used (Wu et al., 2023).

Table 3
Mean fiber diameter for each Box-Behnken experimental design run.

Runs	Independent variables			Response
	A (wt%)	B (wt%)	C (cm)	FD (nm)
1	2	1	9	907
2	4	1	13	685
3	6	3	9	90
4	6	2	5	223
5	4	3	5	139
6	2	3	9	93
7	6	2	13	218
8	2	2	5	144
9	2	2	13	838
10	4	1	5	813
11	4	2	9	885
12	4	3	13	109
13	6	1	9	482
14	4	2	9	910
15	4	2	9	890

A: WPF concentration, B: PCL concentration, C: Tip-collector distance, FD: Mean fiber diameter.

Response variable results of the Box-Behnken experimental design are presented in Table 3, with fibers having diameters ranging between 90 and 910 nm. The smallest diameter (90 nm) was achieved in sample 3, with a concentration of 6 and 3 wt% of whey protein and PCL, respectively, and a tip-collector distance of 9 cm. ANOVA results (Table S3) showed that PCL concentration had the most significant impact on the nanofiber diameter ($p<0.01$). This finding aligns with the relationship between precursor solutions' viscosity and PCL concentration discussed in Section 3.2. Conversely, variations in WPF concentration and collector distance did not significantly affect the fiber diameter ($p>0.05$). da Mata et al. (2022) reported a similar behavior when spinning a blend of chitosan and polyvinyl alcohol, which highlights both the effect of a co-spinnable polymer in green electrospinning and the importance of solution parameters as a means to predict fibers diameter. The determination coefficient (R^2=0.94) and adjusted determination coefficient (R^2_{adj}=0.84) of the fiber diameter model suggested a satisfactory fit of the experimental data with a second-order polynomial equation (Eq. 2). Moreover, the regression model was statistically significant ($p<0.01$) with a non-significant lack of fit ($p>0.05$), which implies good fitness and adequate representation of the data.

$$FD(nm) = 861.8 - 115.4A - 311.6B + 66.3C + 117.2AB - 174.7AC + 24.4BC - 279.2A^2 - 198.4B^2 - 226.8C^2 \quad (2)$$

Finally, the desirability function was used to obtain the optimal conditions for the WPF concentration, PCL concentration, and tip-collector distance that minimized the fiber diameter, while presenting no defects. The optimal conditions of the electrospinning process, with a desirability value of 1, were 6 wt% of WPF, 2 wt% of PCL, and 9 cm of collector distance. At these conditions, the predicted fiber diameter was 103 nm, whereas the validation of the experimental value was 97 nm (Fig. 3a), showing a relative error of 6%. The optimization criterion was selected because it has been reported that smaller fibers have a higher specific surface area (Erben et al., 2021; Ibrahim and Klingner, 2020; Niu et al., 2019), which is often associated with enhanced adsorption properties (Prazeres Mazur et al., 2024). Fig. 3b shows that there is an indirect relationship between fiber diameter and Pb^{2+} adsorption capacity at fixed batch conditions (C_0=2 mmol L^{-1}, 30 °C, pH 5, AD=4 g L^{-1}); WPF/PCL nanofibers obtained at the optimal conditions resulted in the highest Pb removal from water. It is worth mentioning that fibers produced from PCL alone did not adsorb Pb at any tested conditions, suggesting that whey fibrils are responsible for the adsorption properties of the nanofibrous mats. Compared to our previous studies on whey protein spinnability (Ramírez-Rodríguez et al., 2023, Ramírez-Rodríguez et al., 2022), this work demonstrates that uniform nano-scale fibers can also be obtained without addition of toxic reducing agents (β-Me) or organic solvents (THF and DMF) through bromelain hydrolysis and green solvents.

3.4. Characterization of optimal WPF/PCL nanofibers

3.4.1. FT-IR analysis

FT-IR analysis was conducted to investigate the presence of functional groups from whey proteins in the blended nanofibers and to determine the interactions between the pristine precursors (Fig. 4). For PCL, the asymmetric and symmetric stretching vibrations of aliphatic $–CH_2$ were observed at 2944 and 2865 cm^{-1}, respectively. The characteristic absorption band of the carbonyl group C=O appeared at 1725 cm^{-1}, while a stretch vibration corresponding to C-O and C-C bonds was observed with the absorption band located at 1294 cm^{-1}. Symmetric and asymmetric stretching vibrations of C–O–C were observed at 1240 and 1165 cm^{-1}, respectively (Doostmohammadi et al., 2025). The distinct absorption bands of whey proteins were observed in the primary and secondary amide regions via the C=O stretching, with an absorption band at ~1640 cm^{-1} ascribed to β-sheet structures, and a band at 1526 cm^{-1} originated from N-H bending and C–N stretching (Gallardo Salas et al., 2024; Li et al., 2024). In contrast, the broad absorption band at ~3290 cm^{-1} corresponds to the O-H/N-H stretching vibrations. These functional bands of PCL and WPF were also observed in the spectrum of the composite fibers, confirming blending of both materials without the formation of other phases.

3.4.2. XRD analysis

Fig. 5 illustrates the XRD patterns for WPF, PCL and WPF/PCL nanofibrous mats. The semicrystalline nature of PCL was identified by

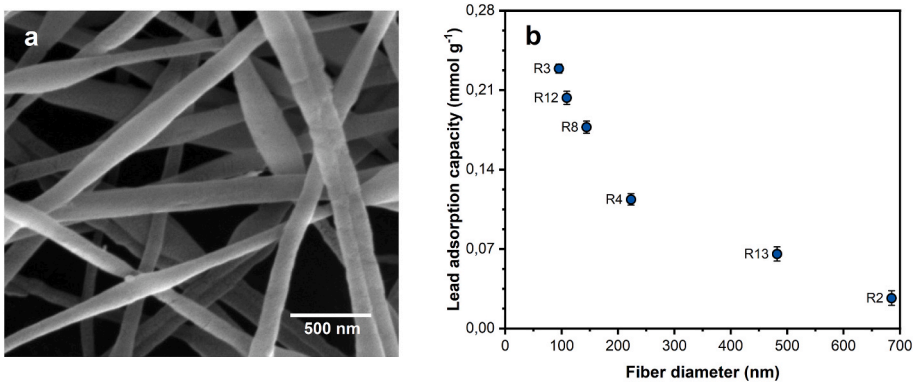

Fig. 3. (a) SEM image of optimal nanofibers observed at 100kX and (b) correlation between fiber diameter of the DOE runs and lead adsorption capacity. Error bars represent the standard deviation of two independent experiments.

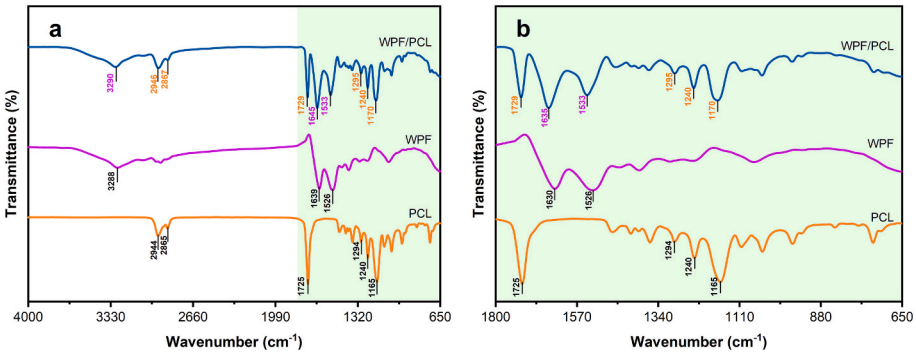

Fig. 4. (a) FT-IR spectra of polycaprolactone (PCL), whey protein fibrils (WPF) and electrospun hybrid composite (WPF/PCL), and (b) zoom between 1800 and 650 cm^{-1}.

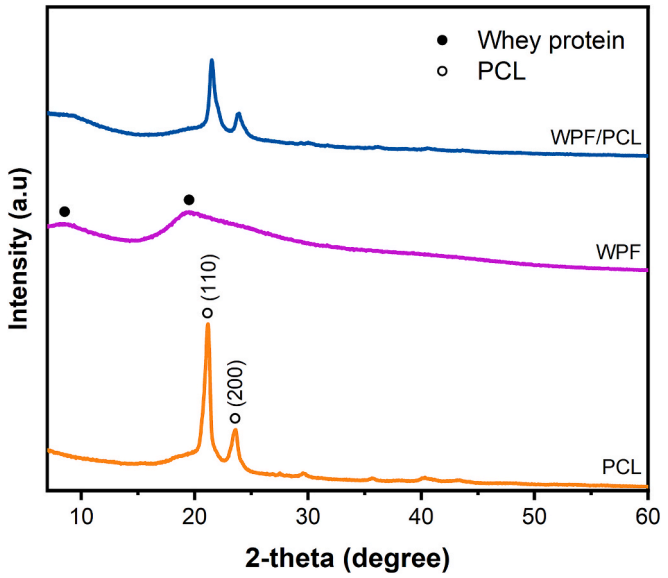

Fig. 5. X-ray diffraction patterns of polycaprolactone (PCL), whey protein fibrils (WPF) and electrospun hybrid composite (WPF/PCL).

two distinct peaks at 21.2° and 23.6° 2θ, which align with the (110) and (200) lattice planes of its orthorhombic form, consistent with literature values (Abdelrazek et al., 2023; Sowmya and Panda, 2022). The diffraction pattern of WPF reveals two broad peaks at approximately 9 and 20° 2θ, signifying the amorphous structure of whey, with the latter representing the average distance of 4.5 Å between β-strands within proteins (Lai et al., 2024). Our earlier research (Gallardo Salas et al., 2024), which involved whey proteins' fibrillation through a traditional acid-heat treatment, also noted a higher intensity of the second peak. This corroborates the fact that the cross-β-structure of whey fibrils can be obtained via enzymatic hydrolysis with bromelain, as observed in the CR absorption spectra. Following the electrospinning process, the XRD pattern of the WPF/PCL nanofibers showed characteristic reflections from both polymers, although with reduced intensities and broader crystalline peaks. This change can be attributed to the successful integration of WPF and PCL due to intermolecular interactions (Ali et al., 2023), along with rapid solvent evaporation during electrospinning due to effective polymer–solvent affinity and adequate tip-collector distance (Yang et al., 2025).

3.4.3. XPS analysis

XPS was conducted to analyze the elemental composition and chemical states of WPF/PCL nanofibers at the surface level. The survey spectrum (Fig. 6a) showed the characteristic signals of carbon (C1s, 84.2%), nitrogen (N1s, 2.7%) and oxygen (O1s, 13.1%). These results are consistent with the elemental composition determined from the EDS spectra (C: 82.7%, N: 2.6%, and O:14.7%) (Fig. S4) and the findings of Ramírez-Rodríguez et al. (2023) for this polymer blend, but on a solvent mixture of THF and DMF, which highlight the potential of green electrospinning. The high resolution scan of C1s depicted four component peaks (Fig. 6b): (1) a peak at 284.8 eV corresponding to aliphatic C-C bonds, (2) a peak at 286.2 eV attributed to the C-O bond of PCL or C-N bond of WPF, (3) a peak at 287.5 eV related to a C=O bond characteristic of the chemical structure of PCL (Sivan et al., 2020), and (4) a peak at 288.7 eV corresponding to an O-C=O bond often observed in whey proteins (Tong et al., 2023). As shown in Fig. 6c, the O1s region was resolved into three peaks: carbonyl (531.7 eV), ether (532.7 eV), and carboxylic (533.9 eV) species. Finally, the high-resolution N1s spectrum of the nanofibrous composite (Fig. 6d) presents two peaks positioned at 400.2 and 402.2 eV, attributed to NH_2 and N-C=O bonds (Li et al., 2024), respectively, reflecting the presence of whey proteins on the backbone chains of PCL.

3.4.4. Surface area

The porous structure of the optimal nanofibers was investigated using N_2 adsorption/desorption isotherms (Fig. S5a). According to the IUPAC classification, the material displays a type IV isotherm, which is typical of mesoporous materials where pore condensation occurs after the initial monolayer-multilayer adsorption (Thommes et al., 2015). The presence of a hysteresis loop at P/P_0=0.93, identified as the H3 form, suggests that the fibers have pores wider than 4 nm, which is corroborated by the pore size distribution depicted in Fig. S5b. Type H3 is also characteristic of non-rigid plate-like pores (Bardestani et al., 2019). The pore sizes were distributed mainly between 1.84 and 32.06 nm, with a mean value of 2.00 nm, which aligns with the width range of mesopores (2–50 nm). The calculated surface area and total pore volume values of WPF/PCL nanofibrous adsorbent were consistent with results reported for different electrospun polymers (Table S4). Particularly, the surface area exhibited herein (2.65 $m^2\ g^{-1}$) compared to our group's previous study on this polymer blend (2.00 $m^2\ g^{-1}$) by Ramírez-Rodríguez et al. (2023), demonstrates that using FA:AA instead of organic solvents can yield fibers with a similar porous structure. The pore width of the composite (~8 nm) exceeded the ionic radius of lead (0.1 nm), which is suitable for increasing the adsorption capacity of the investigated material due to the improved accessibility of metal ions to the fibers' mesopores (Osińska, 2017).

3.4.5. Water contact angle (WCA)

The degree of hydrophilicity and hydrophobicity of a material can be assessed through its contact angle measurement; values below 20° indicate hydrophilic surfaces, whereas values above 90° indicate hydrophobic surfaces (Chen et al., 2025). Fig. S6a shows that upon contact with the water drop, PCL fibers exhibited a WCA of 121.6°, which is

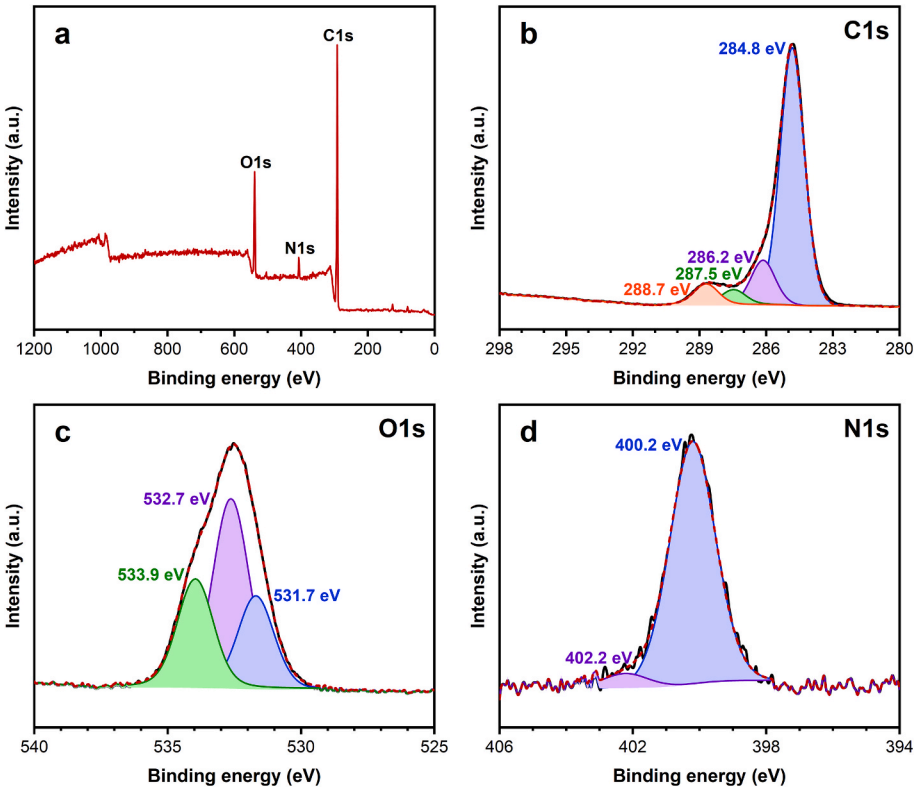

Fig. 6. (a) Survey XPS spectra detailing the surface chemical composition of WPF/PCL fibers and high-resolution XPS spectra for (b) C1s, (c) O1s, and (d) N1s.

comparable to the values obtained by Kim et al. (2017) and Divyasri et al. (2024). The incorporation of whey proteins in the polymer matrix resulted in a significant decrease in contact angle (112.5°), which can be related to polar functional groups identified previously in WPF (amine and hydroxyl groups) that confer a more hydrophobic character to the nanofibers. However, it is important to note that these results differ from the values reported by Ahmed et al. (2016), who evaluated the WCA of WPC/PCL electrospun fibers without any treatment (<84°). These differences reflect the changes in protein structure due to bromelain hydrolysis, as fibril formation unfolds the globular assembly of whey and

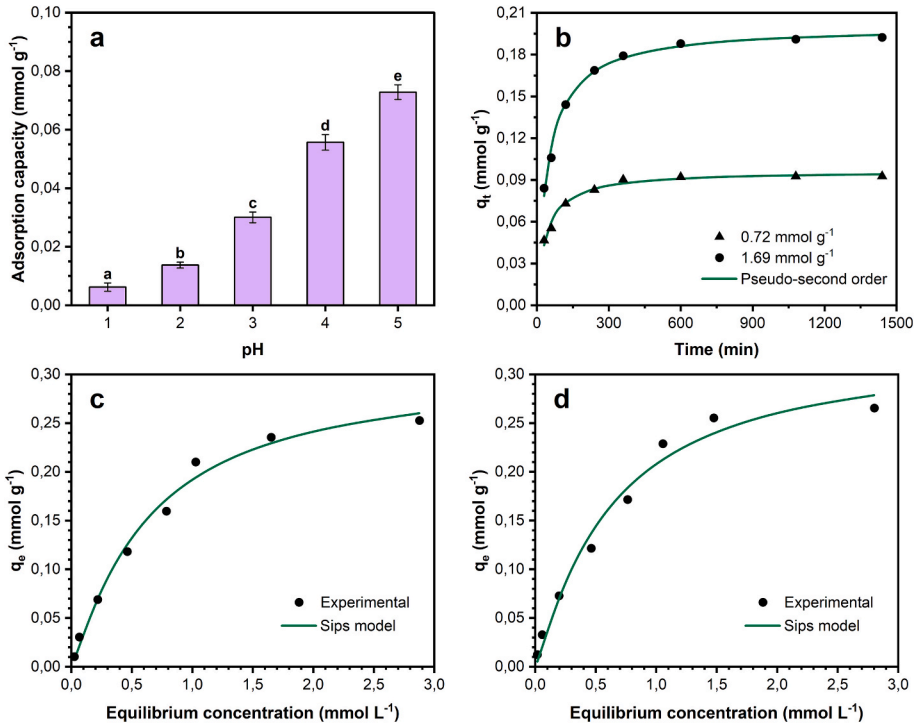

Fig. 7. Adsorption performance of WPF/PCL fibers for Pb^{2+} removal from water. (a) Effect of solution pH on adsorption capacity, (b) kinetic and isotherm modelling at (c) 20 °C and (d) 30 °C. Error bars represent the standard deviation of three independent experiments. Different letters indicate significant difference ($p<0.05$).

exposes its hydrophobic regions (Ali et al., 2023). Similarly, the receding nature of the contact angle over time (Fig. S6b) highlights the increased wettability of nanofibers, facilitating surface and bulk penetration of water and, thus, could improve water flux during continuous adsorption (Ebrahimi et al., 2022).

3.5. Adsorption properties of WPF/PCL nanofibers

3.5.1. Effect of solution pH

Adsorption properties of materials depend on the relationship between their surface charge and the adsorbate charge, both of which are related to the pH of the media. For the adsorbent, the pH at the point of zero charge determines whether the material has a net positive or negative charge; WPF/PCL electrospun fibers are positively charged below pH 5.3 (Fig. S7). On the other hand, the speciation diagram of lead indicates that it mainly exists as cations in the form of Pb^{2+} under acidic conditions. As a result, adsorption hindrance due to electrostatic repulsions take place, behavior evidenced in Fig. 7a. The increasing adsorption capacity at high pH values, owing to the lower H^+ concentration, suggests that the competitive effect between these ions and Pb^{2+} ions decreases in less acidic media (Gallardo Salas et al., 2024). This implies that the Pb removal mechanism is governed by chemical interactions and inner complexation of Pb^{2+} with the nanofibers' functional groups (Merodio-Morales et al., 2022).

3.5.2. Adsorption kinetics

Table 4 displays the results of the non-linear regression parameters, showing that the pseudo-second-order model provided the most accurate data fitting, with R^2>0.98 and the lowest error analysis statistics (*RMSE*<0.03). Consequently, the interaction between Pb^{2+} and the active sites of the nanofibers serves as the rate-limiting mass transfer step (Prasad et al., 2023). This conclusion is supported by the adsorption rate observed in Fig. 7b; equilibrium was achieved at 4 h, after a rapid adsorption phase on the surface's active sites at low adsorbate concentrations, followed by a slower adsorption rate due to saturation of functional groups (Khalil et al., 2023).

3.5.3. Adsorption equilibrium and thermodynamics

Fitting results of lead adsorption on the WPF/PCL fibers are summarized in Table 5, where the Langmuir model demonstrated the best fit to the experimental data, showing the highest determination coefficients (R^2>0.98) and lowest error analysis values (*RMSE*<0.01). According to the Langmuir model, mass transfer occurs predominantly as a monolayer on the adsorbent surface, with energetically homogenous active sites, and is suitable for describing a chemical-driven removal mechanism (Park et al., 2021). However, the overall trend in model fit quality (Langmuir>Redlich-Peterson>Toth>Sips>Dubinin-Radushkevich>-Freundlich), coupled with the fact that *n* values in the three-parameter models deviates from 1, suggests increasing heterogeneity in the adsorption surface, particularly at higher adsorbate concentrations, as

Table 4
Parameters of kinetic models for Pb^{2+} adsorption on WPF/PCL fibers.

Model	Parameter	Concentration (mmol L^{-1}) 0.72	1.69
Pseudo-first order	k_1 (min^{-1})	0.02	0.01
	q_e (*mmol* g^{-1})	0.09	0.18
	R^2	0.92	0.94
	RMSE	0.06	0.06
Pseudo-second order	k_2 (*g* $mmol^{-1}$ min^{-1})	0.28	0.11
	q_e (*mmol* g^{-1})	0.10	0.20
	R^2	0.98	0.99
	RMSE	0.03	0.02
Elovich	α (*mmol* g^{-1} min^{-1})	0.02	0.02
	β (*g* $mmol^{-1}$)	79.25	34.30
	R^2	0.90	0.92
	RMSE	0.07	0.07

Table 5
Parameters of isotherm models for Pb^{2+} adsorption on WPF/PCL fibers.

Model	Parameter	Temperature (°C) 20	30
Langmuir	q_m (*mmol* g^{-1})	0.33	0.35
	K_L (*L* $mmol^{-1}$)	1.31	1.37
	R^2	0.99	0.98
	RMSE	0.00	0.00
Freundlich	K_F (*mmol* g^{-1})	0.17	0.19
	n	0.47	2.18
	R^2	0.94	0.94
	RMSE	0.06	0.05
Dubinin-Radushkevich	q_m (*mmol g-1*)	0.26	0.28
	K_{DR} (mol^2 kJ^{-2})	0.09	0.09
	R^2	0.97	0.96
	RMSE	0.04	0.05
Sips	q_m (*mmol* g^{-1})	0.31	0.33
	K_S (*L* $mmol^{-1}$)	1.57	1.61
	n	1.15	1.14
	R^2	0.99	0.98
	RMSE	0.01	0.01
Redlich-Peterson	a_R	0.53	0.45
	K_R (*L* $mmol^{-1}$)	0.30	0.31
	n	1.43	1.58
	R^2	0.99	0.98
	RMSE	0.01	0.02
Toth	q_m (*mmol* g^{-1})	0.27	0.28
	K_T (*L* $mmol^{-1}$)	1.12	1.06
	n	1.75	2.40
	R^2	0.99	0.98
	RMSE	0.01	0.02

RMSE of the Langmuir model was higher than those of the three-parameter models when C_0>2 mmol L^{-1} (Wang et al., 2024). Adsorption isotherms (Fig. 7c-d) portrayed the L2-type curve according to Gile's isotherm classification for solid–liquid adsorption (Giles et al., 1960), indicating a direct correlation between adsorption capacity and process temperature, which suggests an endothermic process. This finding was further corroborated by the standard enthalpy estimation using the van't Hoff approach. The thermodynamic parameters were $\Delta G<0$ and $\Delta S>0$, indicating spontaneous and entropy increasing traits (Table S5). Moreover, the standard Gibbs free energy change became more negative as the temperature increased, indicating enhanced adsorption spontaneity. Finally, the enthalpy calculated for Pb^{2+} adsorption onto WPF/PCL fibers was found to be 52.1 kJ mol^{-1}, falling within the range of strong physical interactions and possible chemical-based interactions between adsorbent and adsorbate where the formation of metal complexes could be involved (Yanti et al., 2023).

Compared to other electrospun nanofibrous adsorbents (Table 6), WPF/PCL nanofibers exhibited a better adsorption performance, with maximum adsorption capacities of 0.33 and 0.35 mmol g^{-1}, at 20 and 30 °C, respectively. These results underline the complementary roles of both polymers despite the material's relatively low surface area; WPF provides surface functionalities while PCL modulates fiber morphology to enhance accessibility of Pb to active sites, consistent with the results reported by Shi et al. (2025). It is noteworthy that the green electrospinning route presented herein not only yield a highly efficient and environmentally-friendly adsorbent but also improves the cost-effectiveness of the process by relying on abundant, low-cost precursors, particularly whey protein. Indeed, according to the adsorption cost associated with the removal of 1 mmol of adsorbate (Gallardo Salas et al., 2024), the total production cost of WPF/PCL fibers was $7.3 $mmol^{-1}$, with 39% related to reagents and precursors, and 52% to the energy consumption of the electrospinning setup (Table S6).

3.5.4. Adsorption mechanism

Different characterization techniques were carried out to elucidate the surface changes of nanofibrous adsorbent after Pb uptake. The FT-IR spectra (Fig. 8a) presented a shift in position and decreased intensity of

Table 6
Comparison of Pb^{2+} adsorption performance of WPF/PCL fibers with other electrospun fibrous adsorbents.

Adsorbent	FD (nm)	q_m (mmol g^{-1})	Solvent	Ref.
PAN/PANAM/ UiO-66-NH_2 zeolite	133	0.98	N,N-dimethylformamide	(Wang et al., 2025)
PCL	236	0.31	Dichloromethane/ methanol	(Felemban, 2025)
HMO/PAN	415	0.84	N,N-dimethylformamide	(Yadav et al., 2021)
Fe_3O_4/ MWCNTs/ PA6	101	0.24	Dichloromethane/ formic acid	(Bassyouni et al., 2019)
Zeolite/ MWCNTs/ PAN	–	0.03	N,N-dimethylformamide	(Mahmood et al., 2024)
PAN/CS/NaY zeolite	257	0.32	Dimethyl sulfoxide	(Karimzadeh et al., 2023)
Ti3C2Tx MXene/PVP (c)	–	0.06	Ethanol	(Mahar et al., 2023)
WPF/PCL	97	0.35	Formic acid/acetic acid	This work

the absorption bands of the adsorbent, specifically those corresponding to whey proteins. The O-H/N-H vibration and N-C=O stretching signals from the primary and secondary amide regions were displaced from their original positions to 3278, 1635 and 1541 cm^{-1}, respectively, likely due to complexation and chelation between Pb and N (de Aquino et al., 2024). Along with these functional changes, new absorption bands at 2918, 2846, 1368, and 734 cm^{-1}, reported in previous studies (Chen et al., 2024; Soliman et al., 2016), confirmed the successful adsorption of Pb^{2+} ions. XRD patterns shown in Fig. 8b revealed no variation in the position and overall shape of the characteristic reflections of the composite, suggesting no alteration in the crystalline structure of WPF/PCL fibers after adsorption. The presence of new distinct diffraction peaks at 29.4°, 32.0° and 36.2° 2θ, corresponding to the (111), (020) and (002) lattice planes, respectively, could be attributed to lead oxide (ICDD No. 01-078-1665), and thus indicate the participation of oxygenated groups, namely O-H and C=O (Anantha and Kota, 2016).

The XPS characterization results demonstrated the successful removal of Pb from aqueous solutions and validated the interaction between lead ions and the chemistry of nanofibers, as the characteristic peak of Pb4f appeared at ~140 eV, as shown in Fig. 8c. The high-resolution spectra of C1s, N1s, O1s and Pb4f are depicted in Fig. 8d-g. In the C1s spectrum, the binding energy of the nitrogen carbon bond was shifted from 286.2 to 286.3 eV, while the binding energy of the carbonyl bond from the PCL backbone shifted from 287.5 to 287.7 eV. This implies that both functional groups are involved in the adsorption process. The binding energies of O1s decreased slightly for C=O (531.3 eV), C-O (532.3 eV) and –COOH (533.4 eV), owing to the coordination of these species with Pb; electrons are transferred from oxygen to the unoccupied orbital of lead (Wang et al., 2023). The change in the area of these peaks, compared to the O1s spectrum of the composite before adsorption, suggest that there is chemical composition change in the fibers along with the formation of the Pb-O bond, which is consistent with the findings of Esfandiari et al. (2020). Regarding N1s, there were also energy shifts in the deconvoluted peaks of amine and amide bonds, from 400.2 to 399.6 eV, and from 402.2 to 401.2 eV, respectively. Several authors argue that the magnitude of the displacement of peaks before and after adsorption correlates with the binding strength between the adsorbate and the adsorbent active sites (Chen et al., 2024; Liang et al., 2022; Zhang et al., 2020). In this study, Pb has a stronger complexation affinity towards N-containing functional groups, specifically the amide group. Finally, two pairs of symmetrical peaks were obtained in the Pb high-resolution spectrum: (1) a doublet at 138.7 eV ($Pb4f_{7/2}$) and 143.6 eV ($Pb4f_{5/2}$) corresponding to PbO, and (2) a doublet at 139.7 eV ($Pb4f_{7/2}$) and 144.6 eV ($Pb4f_{5/2}$) corresponding to $PbNO_3$. These signals are in line with the binding energies reported in other studies (Esfandiari et al., 2020; Huang et al., 2024; Wang et al., 2023), and corroborate results obtained from FT-IR and XRD analyses.

4. Conclusions

In this study, green electrospinning was used to create uniform WPF/PCL fibers for Pb removal from water. Evaluation of viscosity,

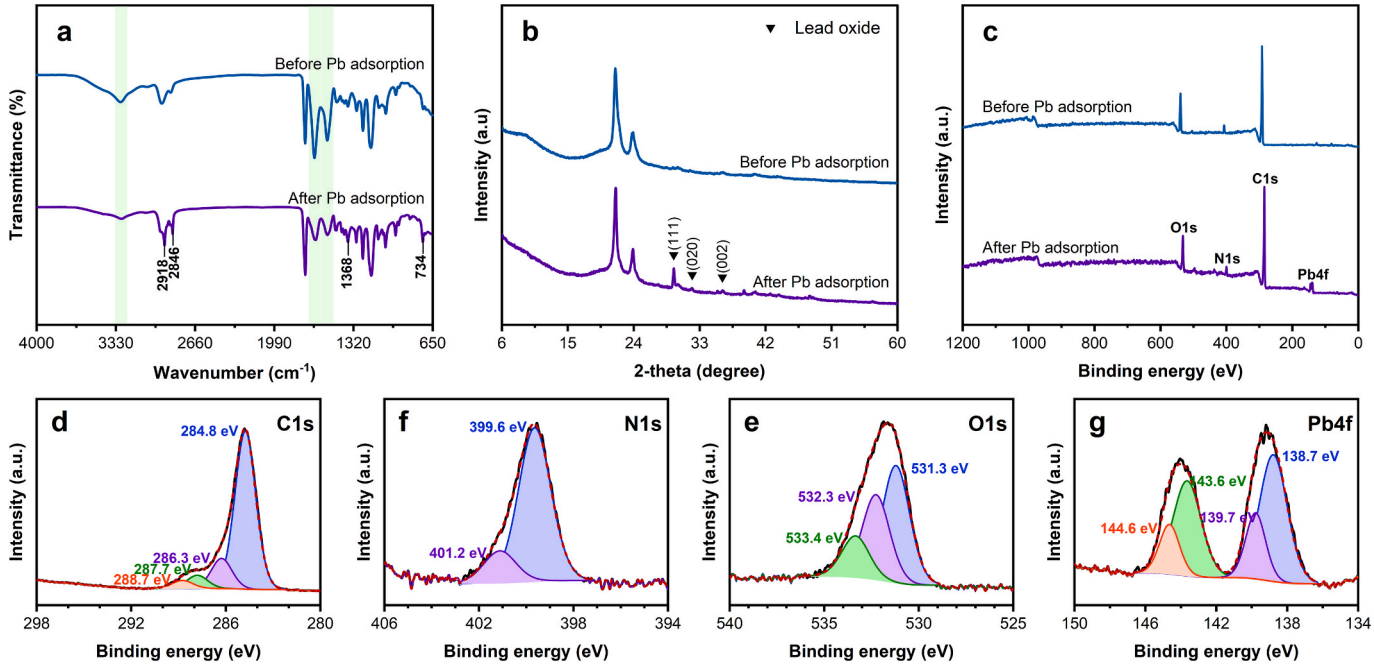

Fig. 8. Comparative analysis of WPF/PCL fibers before and after Pb^{2+} adsorption. (a) FT-IR, (b) XRD, (c) XPS survey spectra and high-resolution XPS spectra of (d) C1s, (e) O1s, (f) N1s and (g) Pb4f.

conductivity, and surface tension of polymer solutions served as a preliminary estimation of their spinnability behavior. The bromelain pretreatment proved to be crucial to spin whey, as its globular native state inhibits adequate chain entanglements, even in the presence of a spinnable polymer such as PCL. The Box-Behnken experimental design validated the importance of polymer concentration in determining the size of fiber diameters and resulted in an optimal configuration to produce beadless nanofibers with a diameter of 97 nm. FT-IR, XRD, and XPS analyses confirmed the coexistence of the protein constituents and PCL in the electrospun nanofiber structure, with whey increasing nanofiber hydrophilicity and wettability, suggesting the potential of the material for continuous adsorption processes. The adsorption kinetics followed the pseudo-second-order model, while the isotherm and thermodynamic analyses suggested a favorable interaction between Pb^{2+} and the functional groups of the fibers via an endothermic process. Physicochemical characterization of the material after adsorption confirmed the binding of Pb into the active sites of the nanofibrous adsorbent. This study provides novel insights into the design of bio-based adsorbents via electrospinning of natural polymers without using toxic organic solvents, so that WPF/PCL nanofibers can be applied as a cost-effective and eco-friendly material for water remediation.

CRediT authorship contribution statement

Mateo Gallardo-Salas: Writing – original draft, Methodology, Investigation, Formal analysis, Conceptualization. **María Ximena Quintanilla Carvajal:** Writing – review & editing, Investigation, Formal analysis. **Didilia Ileana Mendoza-Castillo:** Writing – review & editing, Investigation, Formal analysis. **Adrián Bonilla-Petriciolet:** Writing – review & editing, Supervision. **Martha Cobo:** Writing – review & editing, Funding acquisition. **Carlos Jiménez-Junca:** Writing – review & editing, Supervision, Project administration, Funding acquisition.

Declaration of competing interest

The authors declare that they have no known competing financial interests or personal relationships that could have appeared to influence the work reported in this paper.

Acknowledgements

The authors would like to thank Universidad de La Sabana for the financial support provided (Project code ING-287-2021). Mateo Gallardo-Salas would like to personally acknowledge the Chemical Engineering Department of Instituto Tecnológico de Aguascalientes's support in developing this article.

Appendix A. Supplementary data

Supplementary data to this article can be found online at https://doi.org/10.1016/j.enmm.2026.101134.

Data availability

Data will be made available on request.

References

Abdelrazek, E.M., Hezma, A.M., El-khodary, A., Elzayat, A.M., Rajeh, A., 2023. Modifying of structural, optical, thermal, and mechanical properties of PCL/PMMA biomaterial blend doped with MWCNTs as an application in materials science. J. Inorg. Organomet. Polym Mater. 33, 4117–4126. https://doi.org/10.1007/s10904-023-02625-9.

Aceituno-Medina, M., Lopez-Rubio, A., Mendoza, S., Lagaron, J.M., 2013. Development of novel ultrathin structures based in amaranth (*Amaranthus hypochondriacus*) protein isolate through electrospinning. Food Hydrocoll. 31, 289–298. https://doi.org/10.1016/j.foodhyd.2012.11.009.

Acosta-González, A., Jimenez-Junca, C.A., Gallardo-Salas, M.A., 2025. Management and challenges in access and diagnosis of drinking water services in Rural areas of Latin América. Solutions for Sustain. Through Peri-Urbanization Processes. 289–311. https://doi.org/10.4018/979-8-3693-6089-7.ch010.

Ahmed, S.M., Ahmed, H., Tian, C., Tu, Q., Guo, Y., Wang, J., 2016. Whey protein concentrate doped electrospun poly(epsilon-caprolactone) fibers for antibiotic release improvement. Colloids Surfaces B Biointerfaces 143, 371–381. https://doi.org/10.1016/j.colsurfb.2016.03.059.

Ali, K., Jiang, B., Chen, J., Ashraf, W., Tahir, A.B., 2023. Preparation and structural characterization of pullulan and whey protein isolate-based electrospun nanofiber. Food Biosci. 56. https://doi.org/10.1016/j.fbio.2023.103218.

Aman mohammadi, M., Ramazani, S., Rostami, M., Raeisi, M., Tabibiazar, M., Ghorbani, M., 2019. Fabrication of food-grade nanofibers of whey protein Isolate–Guar gum using the electrospinning method. Food Hydrocoll. 90, 99–104. https://doi.org/10.1016/j.foodhyd.2018.12.010.

Anantha, R.K., Kota, S., 2016. Removal of lead by adsorption with the renewable biopolymer composite of feather (Dromaius novaehollandiae) and chitosan (Agaricus bisporus). Environ. Technol. Innov. 6, 11–26. https://doi.org/10.1016/j.eti.2016.04.004.

Avossa, J., Herwig, G., Toncelli, C., Itel, F., Rossi, R.M., 2022. Electrospinning based on benign solvents: current definitions, implications and strategies. Green Chem. 24, 2347–2375. https://doi.org/10.1039/d1gc04252a.

Ayazi, D., Zandi, M., Ganjloo, A., Dardmeh, N., 2024. Bioactive electrospun zein fibers integrated with ZnO nanoparticles: In vitro investigations. Food Biosci. 62. https://doi.org/10.1016/j.fbio.2024.105343.

Bardestani, R., Patience, G.S., Kaliaguine, S., 2019. Experimental methods in chemical engineering: specific surface area and pore size distribution measurements—BET, BJH, and DFT. Can. J. Chem. Eng. 97, 2781–2791. https://doi.org/10.1002/cjce.23632.

Bassyouni, D., Mohamed, M., El-Ashtoukhy, E.S., El-Latif, M.A., Zaatout, A., Hamad, H., 2019. Fabrication and characterization of electrospun Fe3O4/o-MWCNTs/polyamide 6 hybrid nanofibrous membrane composite as an efficient and recoverable adsorbent for removal of Pb (II). Microchem. J. 149. https://doi.org/10.1016/j.microc.2019.103998.

Behroozi, A.H., Al-Shaeli, M., Vatanpour, V., 2023. Fabrication and modification of nanofiltration membranes by solution electrospinning technique: A review of influential factors and applications in water treatment. Desalination 558, 116638. https://doi.org/10.1016/j.desal.2023.116638.

Biedunkova, O., Kuznietsov, P., 2025. Integration of water management in the assessment of the impact of heavy metals discharge from the power plant with mitigation strategies. Ecol. Ind. 175. https://doi.org/10.1016/j.ecolind.2025.113618.

Bustamante, L.J.A., Maisa, D., de Cerqueira e Silva, M.B., de Paula, A.V., Teixeira, E.M. B., Bassan, J.C., 2022. Enzymatic hydrolysis of Moringa oleifera Lam flour using bromelain and fig by-products as sources of protease. Food Chem. Adv. 1, 100133. https://doi.org/10.1016/j.focha.2022.100133.

Casallas-Ojeda, M., Cabeza, I., Sanchez, N., Caicedo-Concha, D.M., Astals, S., 2024. Cheese whey and dairy manure anaerobic co-digestion at psychrophilic conditions: Technical and environmental evaluation. Environ. Res. 251. https://doi.org/10.1016/j.envres.2024.118525.

Chen, M., Jiang, Q., Li, J., Weng, J., Yan, T., Hu, Y., Wang, X., Zhang, H., 2025. Fabrication and characterization of oleic acid/sesame protein isolate/ poly (vinyl) alcohol core-shell nanofibers: Mitigating lipid oxidation by emulsion electrospinning. Food Chem. 463. https://doi.org/10.1016/j.foodchem.2024.141349.

Chen, Y., Wang, S., Xiang, D., Zhu, M., Liu, X., Zhu, R., Liu, H., Fu, L., 2024. A novel amidoxime-functionalized covalent organic framework adsorbent for efficient lead ion removal: Synthesis and adsorption mechanism. J. Environ. Chem. Eng. 12. https://doi.org/10.1016/j.jece.2024.114206.

Collin, M.S., Venkatraman, S.K., Vijayakumar, N., Kanimozhi, V., Arbaaz, S.M., Stacey, R.G.S., Anusha, J., Choudhary, R., Lvov, V., Tovar, G.I., Senatov, F., Koppala, S., Swamiappan, S., 2022. Bioaccumulation of lead (Pb) and its effects on human: A review. J. Hazard. Mater. Adv. 7. https://doi.org/10.1016/j.hazadv.2022.100094.

Corzo, C.A., Waliszewski, K.N., Welti-Chanes, J., 2012. Pineapple fruit bromelain affinity to different protein substrates. Food Chem. 133, 631–635. https://doi.org/10.1016/j.foodchem.2011.05.119.

Cupp-Enyard, C., 2008. Sigma's Non-specific protease activity assay - Casein as a substrate. J. Vis. Exp. 4–5. https://doi.org/10.3791/899.

Dakhili, S., Abdolalizadeh, L., Hosseini, S.M., Shojaee-Aliabadi, S., Mirmoghtadaie, L., 2019. Quinoa protein: Composition, structure and functional properties. Food Chem. 299. https://doi.org/10.1016/j.foodchem.2019.125161.

de Aquino, R.V.S., de Lucena, P.G.C., Arias, S., Landers, R., Pacheco, J.G.A., Sá da Rocha, O.R., 2024. Influence of terephthalate anion in ZnAl layered double hydroxide on lead ion removal: Adsorption, kinetics, thermodynamics and mechanism. Colloids Surfaces A Physicochem. Eng. Asp. 686. https://doi.org/10.1016/j.colsurfa.2024.133404.

Divyasri, R., Ragupathy, P., Saravanan Kaliaraj, G., Subramanian, B., 2024. Sputtered zirconium based metallic glassy thin films onto electrospun PCL nanofibrous scaffolds for enriching bioactivity. Mater. Chem. Phys. 322. https://doi.org/10.1016/j.matchemphys.2024.129566.

Doostmohammadi, N., Yousefpour, M., Nourbakhsh, M.S., Bahraminasab, M., 2025. Fabrication and characterization of 3D printed PCL/ZrO2/FA scaffolds for bone tissue engineering. Mater. Chem. Phys. 338. https://doi.org/10.1016/j.matchemphys.2025.130659.

Drosou, C., Krokida, M., Biliaderis, C.G., 2018. Composite pullulan-whey protein nanofibers made by electrospinning: Impact of process parameters on fiber morphology and physical properties. Food Hydrocoll. 77, 726–735. https://doi.org/10.1016/j.foodhyd.2017.11.014.

Du, X., Jing, H., Wang, L., Huang, X., Wang, X., Wang, H., 2022. Characterization of structure, physicochemical properties, and hypoglycemic activity of goat milk whey protein hydrolysate processed with different proteases. Lwt 159, 113257. https://doi.org/10.1016/j.lwt.2022.113257.

Du, X., Rashid, S.A., Abdullah, L.C., Rahman, N.A., 2024. Preparation of electrospun cellulose acetate/chitosan membranes for efficient sorption of heavy metals from aqueous solutions. Colloids Surfaces A Physicochem. Eng. Asp. 699. https://doi.org/10.1016/j.colsurfa.2024.134698.

Ebrahimi, F., Nabavi, S.R., Omrani, A., 2022. Fabrication of hydrophilic hierarchical PAN/SiO2 nanofibers by electrospray assisted electrospinning for efficient removal of cationic dyes. Environ. Technol. Innov. 25. https://doi.org/10.1016/j.eti.2021.102258.

Erben, J., Heußner, A., Thiele, S., Kerzenmacher, S., 2021. Activation of electrospun carbon fibers: The effect of fiber diameter on CO2 and steam reaction kinetics. J. Polym. Res. 28. https://doi.org/10.1007/s10965-020-02386-w.

Esfandiari, N., Kashefi, M., Mirjalili, M., Afsharnezhad, S., 2020. Role of silica mid-layer in thermal and chemical stability of hierarchical Fe3O4-SiO2-TiO2 nanoparticles for improvement of lead adsorption: Kinetics, thermodynamic and deep XPS investigation. Mater. Sci. Eng. B 262. https://doi.org/10.1016/j.mseb.2020.114690.

FAO, 2025. Dairy Market Review: Overview of global market developments in 2024. Rome.

Felemban, S.A., 2025. Electrospun polycaprolactone nanofibers reinforced with glutamine and thiosemicarbazide for efficient Pb2+ adsorption from aqueous media. Process Saf. Environ. Prot. 200. https://doi.org/10.1016/j.psep.2025.107445.

Foroumadi, A., Saeedi, M., 2014. Mercaptoethanol, 2-. Encycl. Toxicol. Third Ed. 201–202. https://doi.org/10.1016/B978-0-12-386454-3.00408-5.

Fu, L., Feng, X., Wu, C., Wei, J., Chen, L., Yu, X., Liu, Q., Tang, X., 2025. Bromelain hydrolysis and CaCl2 coordination promote the fibrillation of quinoa protein at pH 7. Food Hydrocoll. 159. https://doi.org/10.1016/j.foodhyd.2024.110659.

Gallardo Salas, M.A., Mendoza-Castillo, D.I., Bonilla-Petriciolet, A., Jiménez-Junca, C., 2024. Functionalized activated carbon with whey protein amyloid fibrils for adsorption of arsenic from water. Environ. Nanotechnology, Monit. Manag. 22. https://doi.org/10.1016/j.enmm.2024.100956.

Giles, C.H., MacEwan, T.H., Nakhwa, S.N., Smith, D., 1960. Studies in Adsorption. Part XI. A system system of classification of solution adsorption isotherms, and its use in diagnosis of adsorption mechanisms and in measurement of specific surface areas of solids. J. Chem. Soc. 846, 3973–3993.

Huang, Y., Peng, Y., Zhang, G., Wu, Z., Li, J., Ding, W., Li, H., An, Y., Ao, L., Shen, Y., Zheng, H., 2024. Synthesis and fabrication of magnetically separable phosphate-modified magnetic chitosan composites for lead(II) selective removal from wastewater. Environ. Res. 258. https://doi.org/10.1016/j.envres.2024.119416.

Ibrahim, H.M., Klingner, A., 2020. A review on electrospun polymeric nanofibers: Production parameters and potential applications. Polym. Test. 90. https://doi.org/10.1016/j.polymertesting.2020.106647.

Karimzadeh, S., HMTShirazi, R., Mohammadi, T., Asadi, A.A., 2023. Polyacrylonitrile (PAN)/Freeze-dried Chitosan (FCS)-NaY zeolite triple layer nanostructure fibrous adsorptive membrane (PAN/FCS-NaY TNAM) for Cu(II) and Pb(II) ions removal from aqueous solutions. Sep. Purif. Technol. 327. https://doi.org/10.1016/j.seppur.2023.124885.

Khalil, A.K.A., Almanassra, I.W., Chatla, A., Ihsanullah, I., Laoui, T., Ali Atieh, M., 2023. Insights into the adsorption of lead ions by Mg-Al LDH doped activated carbon composites: Implications for fixed bed column and batch applications. Chem. Eng. Sci. 281, 119192. https://doi.org/10.1016/j.ces.2023.119192.

Kim, J., Mousa, H.M., Park, C.H., Kim, C.S., 2017. Enhanced corrosion resistance and biocompatibility of AZ31 Mg alloy using PCL/ZnO NPs via electrospinning. Appl. Surf. Sci. 396, 249–258. https://doi.org/10.1016/j.apsusc.2016.10.092.

Kutzli, I., Gibis, M., Baier, S.K., Weiss, J., 2019. Electrospinning of whey and soy protein mixed with maltodextrin – Influence of protein type and ratio on the production and morphology of fibers. Food Hydrocoll. 93, 206–214. https://doi.org/10.1016/j.foodhyd.2019.02.028.

Lai, Y.R., Huang, C.F., How, S.C., Lin, T.H., Wang, S.S.S., 2024. Using titanium dioxide nanoparticle-deposited whey protein isolate amyloid fibrils to photocatalyze the degradation of methylene blue. J. Taiwan Inst. Chem. Eng. 160. https://doi.org/10.1016/j.jtice.2023.105313.

Li, J., Wang, K., Liu, F., Ji, M., Ge, Z., Xie, M., 2025. Charge-enhanced sulfonated block copolymer composite membrane for whey recovery. Sep. Purif. Technol. 363. https://doi.org/10.1016/j.seppur.2025.132081.

Li, J., Yang, Z., Lin, X., Wu, S., Li, G., Li, N., Otter, D., Zhu, F., Hartinger, C., Corke, H., Hemar, Y., 2021. In-flow SAXS investigation of whey protein isolate hydrolyzed by bromelain. Colloids Surfaces A Physicochem. Eng. Asp. 631, 1–7. https://doi.org/10.1016/j.colsurfa.2021.127662.

Li, Z., Zhao, R., Hu, F., Zhang, Y., Dong, B., Lu, P., Song, Z., Wang, H., Zhang, F., Liu, W., Yu, D., Li, H., 2024. Pickering emulsions stabilized by whey protein isolate/nicotinamide mononucleotide complex and their application in pH-responsive drug delivery. Ind. Crop. Prod. 214. https://doi.org/10.1016/j.indcrop.2024.118494.

Liang, C., Zhao, L., Qiao, L., Du, K., 2022. Proteinaceous porous nanofiber membrane-type adsorbent derived from amyloid lysozyme protofilaments for highly efficient lead(II) biologic scavenging. J. Hazard. Mater. 425. https://doi.org/10.1016/j.jhazmat.2021.127886.

Lv, H., Wang, C., Xu, E., Jin, Z., Zhao, H., Yuan, C., Zhao, M., Yu, B., Wu, Z., He, D., Cui, B., 2025. Preparation of starch-based oral fast-disintegrating nanofiber mats for astaxanthin encapsulation and delivery via emulsion electrospinning. Int. J. Biol. Macromol. 289. https://doi.org/10.1016/j.ijbiomac.2024.136466.

Mahar, I., Mahar, F.K., Mahar, N., Memon, A.A., Pirzado, A.A.A., Khatri, Z., Thebo, K.H., Ali, A., 2023. Fabrication and characterization of MXene/carbon composite-based nanofibers (MXene/CNFs) membrane: An efficient adsorbent material for removal of Pb+2 and As+3 ions from water. Chem. Eng. Res. Des. 191, 462–471. https://doi.org/10.1016/j.cherd.2023.02.005.

Mahmood, U., Alkorbi, A.S., Hussain, T., Nazir, A., Qadir, M.B., Khaliq, Z., Faheem, S., Jalalah, M., 2024. Adsorption of lead ions from wastewater using electrospun zeolite/MWCNT nanofibers: kinetics, thermodynamics and modeling study. RSC Adv. 14, 5959–5974. https://doi.org/10.1039/d3ra07720a.

da Mata, G.C., Morais, M.S., de Oliveira, W.P., Aguiar, M.L., 2022. Composition effects on the morphology of PVA/chitosan electrospun nanofibers. Polymers (Basel). 14. https://doi.org/10.3390/polym14224856.

Merodio-Morales, E.E., Mendoza-Castillo, D.I., Bonilla-Petriciolet, A., Reynel-Avila, H.E., Milella, A., di Bitonto, L., Pastore, C., 2022. A novel CO2 activation at room temperature to prepare an engineered lanthanum-based adsorbent for a sustainable arsenic removal from water. Chem. Eng. Res. Des. 185, 239–252. https://doi.org/10.1016/j.cherd.2022.07.003.

Mohamed, M.K., Karuppannan, S.K., Ramalingam, R., Darul, D.R., Vijayalakshmi, S., Arunachalam, K.D., 2025. Fabrication and characterization of electrospun nanofibers infused with hematite nanoparticles for the remediation of heavy metals from aqueous medium. Nano-Structures and Nano-Objects 42. https://doi.org/10.1016/j.nanoso.2025.101452.

Munawar, M.A., Nilsson, F., Schubert, D.W., 2025. Tunable diameter of electrospun fibers using empirical scaling laws of electrospinning parameters. Mater. Chem. Phys. 329. https://doi.org/10.1016/j.matchemphys.2024.130009.

Nguyen, N.H.A., Anema, S.G., Havea, P., Guyomarc'h, F., Wong, M., 2012. Effect of adding low levels of β-mercaptoethanol on the disulphide bonds of κ-casein and β-lactoglobulin solutions. Int. Dairy J. 26, 78–82. https://doi.org/10.1016/j.idairyj.2011.12.005.

Niu, H., Zhou, H., Wang, H., 2019. Electrospinning: an advanced nanofiber production technology, in: Energy Harvesting Properties of Electrospun Nanofibers. pp. 1-1-1–44. https://doi.org/10.1088/978-0-7503-2005-4ch1.

Osińska, M., 2017. Removal of lead(II), copper(II), cobalt(II) and nickel(II) ions from aqueous solutions using carbon gels. J. Sol-Gel Sci. Technol. 81, 678–692. https://doi.org/10.1007/s10971-016-4256-0.

Park, J.-H., Lee, J.-H., Lee, S.-L., Hwang, S.-W., Seo, D.-C., 2021. Adsorption behavior of arsenic onto lignin-based biochar decorated with zinc. Colloids Surfaces A Physicochem. Eng. Asp. 626, 127095. https://doi.org/10.1016/j.colsurfa.2021.127095.

Perez-Puyana, V.M., Romero, A., Guerrero, A., Moroni, L., Wieringa, P.A., 2025. Enabling low molecular weight electrospinning through binary solutions of polymer blends. Next Mater. 6, 100306. https://doi.org/10.1016/j.nxmate.2024.100306.

Prasad, G., Lin, X., Liang, J., Yao, Y., Tao, T., Liang, B., Lu, S.G., 2023. Fabrication of intra porous PVDF fibers and their applications for heavy metal removal, oil absorption and piezoelectric sensors. J. Mater. 9, 174–182. https://doi.org/10.1016/j.jmat.2022.08.003.

Prazeres Mazur, L., Reis Ferreira, R., Felix da Silva Barbosa, R., Henrique Santos, P., Barcelos da Costa, T., Gurgel Adeodato Vieira, M., da Silva, A., dos Santos Rosa, D., Helena Innocentini Mei, L., 2024. Development of novel biopolymer membranes by electrospinning as potential adsorbents for toxic metal ions removal from aqueous solution. J. Mol. Liq. 395. https://doi.org/10.1016/j.molliq.2023.123782.

Ramírez-Rodríguez, L.C., Mendoza-Castillo, D.I., Bonilla-Petriciolet, A., Jiménez-Junca, C., 2023. Comparison of adsorption performance of nanocomposite materials of whey protein nanofibrils, polycaprolactone and activated carbon for mercury removal. Environ. Nanotechnology, Monit. Manag. 20. https://doi.org/10.1016/j.enmm.2023.100826.

Ramírez-Rodríguez, L.C., Quintanilla-Carvajal, M.X., Mendoza-Castillo, D.I., Bonilla-Petriciolet, A., Jiménez-Junca, C., 2022. Preparation and characterization of an electrospun whey protein/polycaprolactone nanofiber membrane for chromium removal from water. Nanomaterials 12, 2744. https://doi.org/10.3390/nano12162744.

Refate, A., Mohamed, Y., Mohamed, M., Sobhy, M., Samhy, K., Khaled, O., Eidaroos, K., Batikh, H., El-Kashif, E., El-Khatib, S., Mehanny, S., 2023. Influence of electrospinning parameters on biopolymers nanofibers, with emphasis on cellulose & chitosan. Heliyon 9. https://doi.org/10.1016/j.heliyon.2023.e17051.

Ricaurte, L., Santagapita, P.R., Díaz, L.E., Quintanilla-Carvajal, M.X., 2020. Edible gelatin-based nanofibres loaded with oil encapsulating high-oleic palm oil emulsions. Colloids Surfaces A Physicochem. Eng. Asp. 595, 124673. https://doi.org/10.1016/j.colsurfa.2020.124673.

Rostamabadi, H., Assadpour, E., Tabarestani, H.S., Falsafi, S.R., Jafari, S.M., 2020. Electrospinning approach for nanoencapsulation of bioactive compounds; recent advances and innovations. Trends Food Sci. Technol. 100, 190–209. https://doi.org/10.1016/j.tifs.2020.04.012.

Rostami, M., Beheshtizadeh, N., Ranjbar, F.E., Najafi, N., Ahmadi, A., Ahmadi, P., Rostamabadi, H., Pazhouhnia, Z., Assadpour, E., Mirzanajafi-Zanjani, M., Kisomi, M. F., Kharazmi, M.S., Jafari, S.M., 2023. Recent advances in electrospun protein fibers/nanofibers for the food and biomedical applications. Adv. Colloid Interface Sci. 311, 102827. https://doi.org/10.1016/j.cis.2022.102827.

Rout, P., Chkraborty, C., Hossain, S., 2024. Functional characterization of enzyme-hydrolysed soy and whey protein isolates: A comparative approach. Food Chem, Adv, p. 5.

Saghaee, R., Ariaii, P., Motamedzadegan, A., 2025. Development of electrospun whey protein isolate nanofiber mat for omega-3 nanoencapsulation: Microstructural and

physical property analysis. Int. J. Biol. Macromol. 301. https://doi.org/10.1016/j.ijbiomac.2025.140273.
Saisree, S., Nair, A.S., Dais, E., Sandhya, K.Y., 2025. Electrochemical sensors for monitoring water quality: Recent advances in graphene quantum dot-based materials for the detection of toxic heavy metal ions Cd(II), Pb(II) and Hg(II) with their mechanistic aspects. J. Environ. Chem. Eng. 13. https://doi.org/10.1016/j.jece.2025.116545.
Shi, S., Guo, Z., Liu, Z., Yang, A., You, Y., Jiang, L., Deng, H., Gao, P., 2025. Preparation of self-supporting flexible NiFe2O4 fibers and their adsorption performance for Pb (II). J. Magn. Magn. Mater. 629. https://doi.org/10.1016/j.jmmm.2025.173327.
Sivan, M., Madheswaran, D., Asadian, M., Cools, P., Thukkaram, M., Van Der Voort, P., Morent, R., De Geyter, N., Lukas, D., 2020. Plasma treatment effects on bulk properties of polycaprolactone nanofibrous mats fabricated by uncommon AC electrospinning: A comparative study. Surf. Coatings Technol. 399. https://doi.org/10.1016/j.surfcoat.2020.126203.
Soleimanifar, M., Jafari, S.M., Assadpour, E., 2020. Encapsulation of olive leaf phenolics within electrosprayed whey protein nanoparticles; production and characterization. Food Hydrocoll. 101. https://doi.org/10.1016/j.foodhyd.2019.105572.
Soliman, A.M., Elwy, H.M., Thiemann, T., Majedi, Y., Labata, F.T., Al-Rawashdeh, N.A.F., 2016. Removal of Pb(II) ions from aqueous solutions by sulphuric acid-treated palm tree leaves. J. Taiwan Inst. Chem. Eng. 58, 264–273. https://doi.org/10.1016/j.jtice.2015.05.035.
Soon, W.L., Peydayesh, M., Mezzenga, R., Miserez, A., 2022. Plant-based amyloids from food waste for removal of heavy metals from contaminated water. Chem. Eng. J. 445, 136513. https://doi.org/10.1016/j.cej.2022.136513.
Sowmya, B., Panda, P.K., 2022. Electrospinning of poly(ε-caprolactone) (PCL) and poly ethylene glycol (PEG) composite nanofiber membranes using methyl ethyl ketone (MEK) and N N'-dimethyl acetamide (DMAc) solvent mixture for anti-adhesion applications. Mater. Today Commun. 33. https://doi.org/10.1016/j.mtcomm.2022.104718.
Stie, M.B., Kalouta, K., da Cunha, C.F.B., Feroze, H.M., Vetri, V., Foderà, V., 2022. Sustainable strategies for waterborne electrospinning of biocompatible nanofibers based on soy protein isolate. Sustain. Mater. Technol. 34. https://doi.org/10.1016/j.susmat.2022.e00519.
Thommes, M., Kaneko, K., Neimark, A.V., Olivier, J.P., Rodriguez-Reinoso, F., Rouquerol, J., Sing, K.S.W., 2015. Physisorption of gases, with special reference to the evaluation of surface area and pore size distribution (IUPAC Technical Report). Pure Appl. Chem. 87, 1051–1069. https://doi.org/10.1515/pac-2014-1117.
Tong, Y., Yue, Y., Hou, M., Zhang, T., Lu, Z., Yang, L., Liu, P., 2023. Hydration effect of whey protein treated by glow discharge plasma. Innov. Food Sci. Emerg. Technol. 87. https://doi.org/10.1016/j.ifset.2023.103409.
Unesco, 2024. The united nations world water development report 2024: Water for prosperity and peace. United Nations. https://doi.org/10.1596/29263.
Uribe-Velázquez, T., Díaz-Vázquez, D., Barajas-Álvarez, P., González-López, M.E., Gradilla-Hernández, M.S., Garcia-Amezquita, L.E., Carrillo-Nieves, D., García-Cayuela, T., 2025. From waste to value: Mitigating the environmental impact of whey in Jalisco. Mexico. J. Clean. Prod. 501. https://doi.org/10.1016/j.jclepro.2025.145334.
Wang, H., Miao, D., Yu, Y., Zhang, Z., Zhu, Y., Wang, Q., 2024. PVA/PAA/DMTD electrospun nanofibrous membrane for the selective adsorption of Pb(II) ions in liquid foods. iScience 27. https://doi.org/10.1016/j.isci.2023.108737.
Wang, J., Zhan, J., Zhou, H., Yi, X., Liu, Y., 2023. Removal of lead from aqueous solution by synergistic interaction between LiCoO2 and tourmaline: Synthesis, characterization and mechanism investigation. Appl. Surf. Sci. 631. https://doi.org/10.1016/j.apsusc.2023.157485.
Wang, Q., Shao, Z., Shen, R., Chen, R., Gui, Z., Li, G., Liu, Y., Zheng, G., Sui, J., Qi, Y., Song, W., 2024. Preparation of ethyl cellulose bimodal nanofibrous membrane by green electrospinning based on molecular weight regulation for high-performance air filtration. Int. J. Biol. Macromol. 275. https://doi.org/10.1016/j.ijbiomac.2024.133411.
Wang, X., Zhang, D., Ji, Z., Xu, Y., Zhao, Y., Xie, M., 2025. Facile fabrication of PAN/PAMAM@UiO-66-NH2 composite nanofiber membranes for enhanced Pb2+ adsorption. J. Water Process Eng. 71. https://doi.org/10.1016/j.jwpe.2025.107022.
Wilk, S., 2021. Advances in fabricating the electrospun biopolymer-based biomaterials. J. Fuctional Biomater. 12.
Wu, S., Shi, W., Li, K., Cai, J., Xu, C., Gao, L., Lu, J., Ding, F., 2023. Chitosan-based hollow nanofiber membranes with polyvinylpyrrolidone and polyvinyl alcohol for efficient removal and filtration of organic dyes and heavy metals. Int. J. Biol. Macromol. 239, 124264. https://doi.org/10.1016/j.ijbiomac.2023.124264.
Xu, J., Zhao, X., Tang, M., Ban, Q., Zhao, R., An, J., Wang, M., 2025. Tannic acid-mediated reconfiguration of oat globulin fibril-based hydrogels for quercetin encapsulation: construction, mechanism and performance. Food Chem.: X 30. https://doi.org/10.1016/j.fochx.2025.102930.
Yadav, P., Farnood, R., Kumar, V., 2021. HMO-incorporated electrospun nanofiber recyclable membranes: Characterization and adsorptive performance for Pb(II) and As(V). J. Environ. Chem. Eng. 9. https://doi.org/10.1016/j.jece.2021.106507.
Yang, Q., Wang, Y.R., Du, Y.N., Chen, H.Q., 2023. Comparison of the assembly behavior and structural characteristics of arachin and conarachin amyloid-like fibrils. Food Hydrocoll. 138, 108479. https://doi.org/10.1016/j.foodhyd.2023.108479.
Yang, W., Wang, A., Wu, Y., Zhou, Y., Hu, Y., 2025. PCL/soy peptide nanofibers incorporated with riboflavin/HP-β-CD assemblies for improving fruit storage quality. Food Chem. 464. https://doi.org/10.1016/j.foodchem.2024.141730.
Yanti, I., Sationo, P.P., Winata, W.F., Anugrahwati, M., Anas, A.K., Swasono, Y.A., 2023. Effectiveness of activated carbon magnetic composite from banana peel (Musa acuminata) for recovering iron metal ions. Case Stud. Chem. Environ. Eng. 8, 100378. https://doi.org/10.1016/j.cscee.2023.100378.
Zhang, Q., Lin, J., Dong, Y., Sun, F., 2023. Investigation of the rheological response of a bio-liquefied formaldehyde resin-based precursor for electrospinning. Colloids Surfaces A Physicochem. Eng. Asp. 661, 130950. https://doi.org/10.1016/j.colsurfa.2023.130950.
Zhang, Q., Zhang, S., Zhao, Z., Liu, M., Yin, X., Zhou, Y., Wu, Y., Peng, Q., 2020. Highly effective lead (II) removal by sustainable alkaline activated β-lactoglobulin nanofibrils from whey protein. J. Clean. Prod. 255. https://doi.org/10.1016/j.jclepro.2020.120297.
Zhao, Y.M., Li, Y., Ma, H., He, R., 2023. Effects of ultrasonic-assisted pH shift treatment on physicochemical properties of electrospinning nanofibers made from rapeseed protein isolates. Ultrason. Sonochem. 94. https://doi.org/10.1016/j.ultsonch.2023.106336.
Zhong, J., Mohan, S.D., Bell, A., Terry, A., Mitchell, G.R., Davis, F.J., 2018. Electrospinning of food-grade nanofibres from whey protein. Int. J. Biol. Macromol. 113, 764–773. https://doi.org/10.1016/j.ijbiomac.2018.02.113.
Zhu, F., Zheng, Y.M., Zhang, B.G., Dai, Y.R., 2021. A critical review on the electrospun nanofibrous membranes for the adsorption of heavy metals in water treatment. J. Hazard. Mater. 401, 123608. https://doi.org/10.1016/j.jhazmat.2020.123608.